

# Development and Evolution of Nitrogen Dioxide Gas Sensor Based on Silver-Doped Cerium Oxide Nanoparticles

Kavitha Bharathi K\*, Azha. Periasamy\*\*, Paramaguru PV, and Maheswaran R

<sup>1</sup>Ph.D. Research Scholar, Department of Electronics and instrumentation, Bharathiar University, Coimbatore, Tamil Nadu. India

<sup>2</sup>Associate Professor, Department of Electronics and Instrumentation, Bharathiar University, Coimbatore, Tamil Nadu. India

<sup>3&4</sup> Department of Electronics and Instrumentation, Bharathiar University, Coimbatore, Tamil Nadu. India

<sup>1</sup> [kavithabarathi55@gmail.com](mailto:kavithabarathi55@gmail.com), <sup>2</sup> [azhaperiasamy65@buc.edu.in](mailto:azhaperiasamy65@buc.edu.in), <sup>3</sup> [paramaguru.ei@buc.edu.in](mailto:paramaguru.ei@buc.edu.in), and <sup>4</sup> [mahes94@gmail.com](mailto:mahes94@gmail.com).

## Abstract

The cerium oxide (CeO<sub>2</sub>) and silver nanoparticle-doped cerium oxide (CeO<sub>2</sub>:Ag NPs) were successfully synthesized using thermal vacuum evaporation. Structural analysis confirmed a polycrystalline cubic Cerianite structure, and the crystallite size was found to decrease from 8.6 nm to 6.8 nm upon Ag doping. Optical measurements showed strong absorption for pure CeO<sub>2</sub> at 400 nm, while doping with Ag NPs caused a slight blue shift and increased the optical band gap to 2.9 eV. The incorporation of Ag NPs significantly enhanced the NO<sub>2</sub> sensing performance, with the doped film showing a response of 134% to 5 ppm NO<sub>2</sub> at 25 °C which is 1.4 times higher than the undoped counterpart. The sensing mechanism, along with the repeatability, selectivity, and stability of the developed sensors, was comprehensively studied.

## 1.INTRODUCTION

Recent developments in nanomaterials have led to notable improvements in gas sensor performance, largely due to their high surface-to-volume ratios. Nanostructured semiconductor oxides offer great potential for enhancing sensor sensitivity, selectivity, and operating efficiency, particularly by reducing working temperatures an ongoing challenge in chemiresistive sensing. Numerous metal oxide semiconductors such as SnO<sub>2</sub> [2], In<sub>2</sub>O<sub>3</sub> [3], TeO<sub>2</sub> [4], MoO<sub>3</sub> [5], and Fe<sub>2</sub>O<sub>3</sub> [6] have been widely investigated for their simple fabrication methods, chemical diversity, low cost, and favorable electrical properties. Cerium oxide (CeO<sub>2</sub>), a rare-earth metal oxide, has also shown great promise in gas sensing applications and is widely used in areas such as photodetection [7], fuel cells [8], catalysis [9], and biomedical fields [10]. This is attributed to its unique electronic structure and the mobility of its 4f electrons [11]. In an ideal CeO<sub>2</sub> crystal, cerium and oxygen ions are arranged in a face-centered cubic structure, with each cerium atom surrounded by eight oxygen atoms. Nanostructured CeO<sub>2</sub> exhibits a higher Ce<sup>3+</sup>/Ce<sup>4+</sup> ratio compared to its bulk form, resulting in a greater number of surface oxygen vacancies that facilitate rapid redox reactions [13,14]. This redox behavior, involving transitions between Ce<sup>4+</sup> (CeO<sub>2</sub>) and Ce<sup>3+</sup> (Ce<sub>2</sub>O<sub>3</sub>), makes CeO<sub>2</sub> particularly suitable for gas sensing.

Unlike conventional semiconductor gas sensors that rely solely on oxygen adsorption and electron transfer at the surface, CeO<sub>2</sub> sensors benefit from their inherent oxygen mobility. However, limitations such as low selectivity and stability still exist. These issues can be addressed by incorporating noble metals such as Ag, Au, Pd, Pt, or Ru which enhance sensor performance by promoting catalytic activity and electron transfer [15]. Nitrogen dioxide (NO<sub>2</sub>) is a highly toxic and reactive pollutant. Even at concentrations as low as 10–

20 ppm, NO<sub>2</sub> can cause respiratory irritation, while levels of 25–50 ppm may lead to serious conditions like pulmonary edema and pneumonia [16]. Therefore, the development of reliable NO<sub>2</sub> sensors capable of detecting low concentrations at room temperature is critical. This study focuses on improving the sensitivity and selectivity of CeO<sub>2</sub>-based NO<sub>2</sub> sensors by doping the films with silver nanoparticles. The sensors were fabricated via thermal vacuum evaporation and systematically characterized for structural, morphological, and optical properties. The effects of Ag doping on the gas sensing response, selectivity, and long-term stability were also thoroughly evaluated. A comparison with existing CeO<sub>2</sub>-based sensors (Table 1) shows that the proposed sensor exhibits enhanced performance, especially at low operating temperatures and gas concentrations.

## **II. EXPERIMENTAL METHODS AND MATERIALS**

### **MATERIALS AND FILM DEPOSITION**

High-purity cerium oxide (CeO<sub>2</sub>) powder (99.995%) was obtained from Merck, while silver (Ag) powder (purity >99.9%) was sourced from Sigma-Aldrich. Both materials were used without further purification. Thin films were deposited using the thermal physical vapor deposition technique, employing an Edwards Auto 306 system. The deposition setup included a bell-jar-type chamber equipped with a rotary and diffusion pump to achieve high vacuum conditions. A tungsten boat, cleaned with ethanol and dried using nitrogen gas, was used to contain the source material. The glass substrates were positioned above the tungsten boat inside the chamber. After evacuating the chamber to a vacuum level of 3 Torr, a direct current of 3 A was initially applied for 15 s to preheat the CeO<sub>2</sub> powder, followed by an increase to 7 A to initiate evaporation. For the undoped CeO<sub>2</sub> film, 0.217 g of CeO<sub>2</sub> powder was used. In the case of the Ag-doped CeO<sub>2</sub> film, 0.25 wt% of silver powder was mixed with CeO<sub>2</sub> powder and ground using a PM 100 nano ball mill. The composite powder was then deposited under the same conditions as pure CeO<sub>2</sub>.

### **Film Characterization**

The structural properties of the deposited thin films, including phase identification and crystallite size estimation, were investigated using a Shimadzu XRD-6000 X-ray diffractometer. Surface morphology was examined via scanning electron microscopy, while atomic force microscopy was employed to assess topographical features and particle size distribution. Photoluminescence (PL) spectra were recorded at room temperature using an SPX500 spectrometer with a 320 nm excitation source. Optical absorbance and band gap analysis were conducted using a Lambda 900 UV–Vis spectrophotometer across the 200–800 nm wavelength range. Film thicknesses were measured using a Bruker-Dektak Filmetric reflectometer and were found to be approximately 118 nm for CeO<sub>2</sub> and 124 nm for CeO<sub>2</sub>:Ag films.

### **Gas Sensing Setup and Measurements**

The gas sensing experiments were carried out using a 225 cm<sup>3</sup> stainless steel test chamber equipped with an electric heater and a thermocouple for precise temperature control. A mass flow controller regulated the flow of the analyte gas, NO<sub>2</sub>, diluted in dry air. Aluminum electrodes were deposited on the thin films using a 15 × 15 mm aluminum mask through thermal evaporation. A bias voltage of 5 V was applied across the electrodes to monitor resistance changes during gas exposure. To generate various NO<sub>2</sub> concentrations, dry air was maintained at a constant flow rate of 2 SLPM (standard liters per minute), and NO<sub>2</sub> was introduced by adjusting its partial flow while keeping the total rate unchanged. The sensor's baseline resistance was recorded in pure dry air, and the response was measured after exposure to the gas mixture. Selectivity tests

were conducted by introducing different gases into the chamber, and their concentrations were also controlled via the mass flow controller.

### III. RESULTS AND DISCUSSION

#### Structural Analysis

Figure 1 presents the X-ray diffraction (XRD) patterns of both pure  $\text{CeO}_2$  and Ag-doped  $\text{CeO}_2$  thin films. The diffraction peaks observed at  $2\theta$  values of  $28.52^\circ$ ,  $32.99^\circ$ ,  $47.40^\circ$ ,  $56.23^\circ$ ,  $58.92^\circ$ ,  $69.42^\circ$ ,  $76.62^\circ$ ,  $79.32^\circ$ , and  $88.68^\circ$  correspond to the (111), (002), (220), (311), (222), (400), (331), (420), and (422) planes, respectively, confirming a polycrystalline cubic fluorite structure of  $\text{CeO}_2$  as per JCPDS card No. 96-900-9009. Upon doping with Ag, additional peaks appeared at  $2\theta = 44.4^\circ$  and  $47.56^\circ$ , corresponding to the (111) and (200) planes of metallic silver, consistent with JCPDS card No. 96-101-0605. The presence of metallic Ag suggests the formation of a metal–semiconductor interface, which plays a critical role in forming a Schottky barrier, thereby enhancing the sensing response, as discussed later.

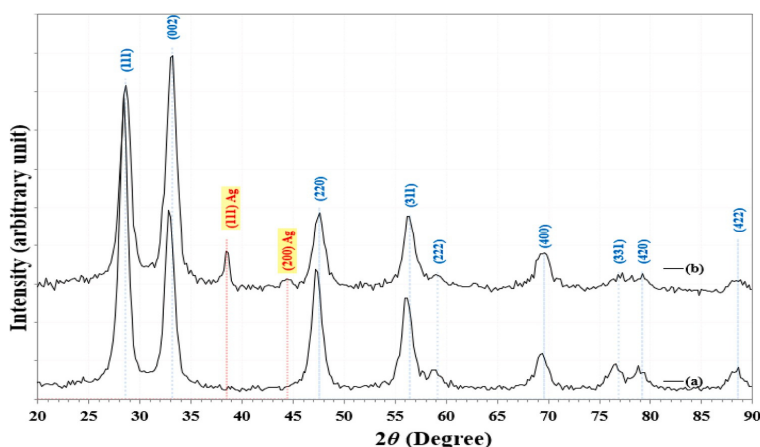


**Fig. 1.** X-ray diffraction patterns (a) as-deposited  $\text{CeO}_2$  and (b)  $\text{CeO}_2\text{:Ag}$  thin films.

Interestingly, the preferred orientation of crystal growth shifts from the (111) plane in pure  $\text{CeO}_2$  to the (002) plane in the Ag-doped sample. This indicates that the incorporation of Ag NPs influences the crystallographic orientation of the films. Figure 1 illustrates the Rietveld refinement of the XRD data for both samples, showing a good match with standard reference patterns. Using the Scherrer equation, the crystallite sizes were calculated based on the full width at half maximum (FWHM) values. Detailed results, including interplanar spacing and crystallite size, are summarized in Table 1.

**Table 1**

Comparison of  $\text{CeO}_2$  nanostructures-based operating temperature, gas concentration, and gas sensing performance.

Sensing layer	Deposition method	Gas type/concentration (ppm)	Operating temperature ( $^\circ\text{C}$ )	Sensor response
$\text{CeO}_2$ nanoparticles	Dip-coating	$\text{NO}_2/50$	300	8.8
$\text{CeO}_2$ nanoparticles	Chemical precipitation	$\text{NO}_2/40$	100	2.2
$\text{CeO}_2$ /graphene nanoparticles	Hydrothermal reactions	$\text{NO}_2/200$	200	48
$\text{CeO}_2/\text{ZnO}$ nanorod-array	Anodic electrodeposition	$\text{NO}_2/5$	120	26.33
$\text{CeO}_2$ /Graphene nanotubes	Hydrothermal	$\text{NO}_2/100$	Room temperature	33
$\text{CeO}_2$ nanoparticles	Co-precipitation	$\text{CO}_2/800$	250	43
$\text{CeO}_2$ Nanospheres	Reversed micelles	$\text{CO}/30$	400	52
$\text{CeO}_2$ nanorods	Solvothermal	$\text{H}_2/1000$	100	5.32
$\text{CeO}_2$ spherical nanostructure	Co-precipitation	$\text{C}_3\text{H}_8\text{O}/100$	Room temperature	139
$\text{CeO}_2\text{:Ag}$	Thermal evaporation	$\text{NO}_2/5$	25	134

The lattice constants ( $a = b = c$ ) of the as-deposited  $\text{CeO}_2$  and  $\text{CeO}_2\text{:Ag}$  thin films were calculated using Equation [25], based on the slope of the linear plot of d-spacing versus  $1/\sqrt{h^2 + k^2 + l^2}$ , as shown in Figure 2. For pure  $\text{CeO}_2$ , the lattice constant was found to be 5.4184 nm, which decreased to 5.3924 nm after Ag doping. This reduction is attributed to the substitution of smaller Ag atoms into the  $\text{CeO}_2$  lattice, which slightly contracts the crystal structure while remaining close to standard lattice parameter values. Field-emission scanning electron microscopy (FE-SEM) images of the pure and Ag-doped  $\text{CeO}_2$  thin films are shown in Figure 2. The undoped  $\text{CeO}_2$  film (Fig. 2a) exhibits a cauliflower-like surface morphology composed of aggregated, spherical particles with diameters ranging from 14.1 nm to 33.9 nm. Upon doping with silver, the particle size is reduced to approximately 13.5 nm, and the surface transforms into a porous, island-clustered structure with clearly defined grain boundaries (Fig. 2b). This porous texture enhances the surface area available for gas adsorption, thereby improving gas film interactions and sensing performance.

Energy-dispersive X-ray spectroscopy (EDX) analysis, shown in Fig. 2c, confirms the presence of cerium, oxygen, and silver elements in the doped film, verifying the successful incorporation of Ag NPs into the  $\text{CeO}_2$  matrix. Elements such as Na, Mg, and Si—originating from the glass substrate—were also detected. Three-dimensional AFM images and grain size distribution plots are presented in Figure 3. The undoped  $\text{CeO}_2$  film (Fig. 3a) shows a wide grain size distribution with an average particle diameter of 128 nm. After Ag doping (Fig. 3b), the grain size is significantly reduced to an average of 44 nm, with a narrower distribution, indicating improved uniformity. Moreover, Ag incorporation increases the root mean square (RMS) surface roughness from 13.46 nm to 24.94 nm and the average surface roughness from 10.62 nm to 17.78 nm. This enhancement in surface roughness is beneficial for gas sensing, as it promotes greater surface activity and improves analyte adsorption.

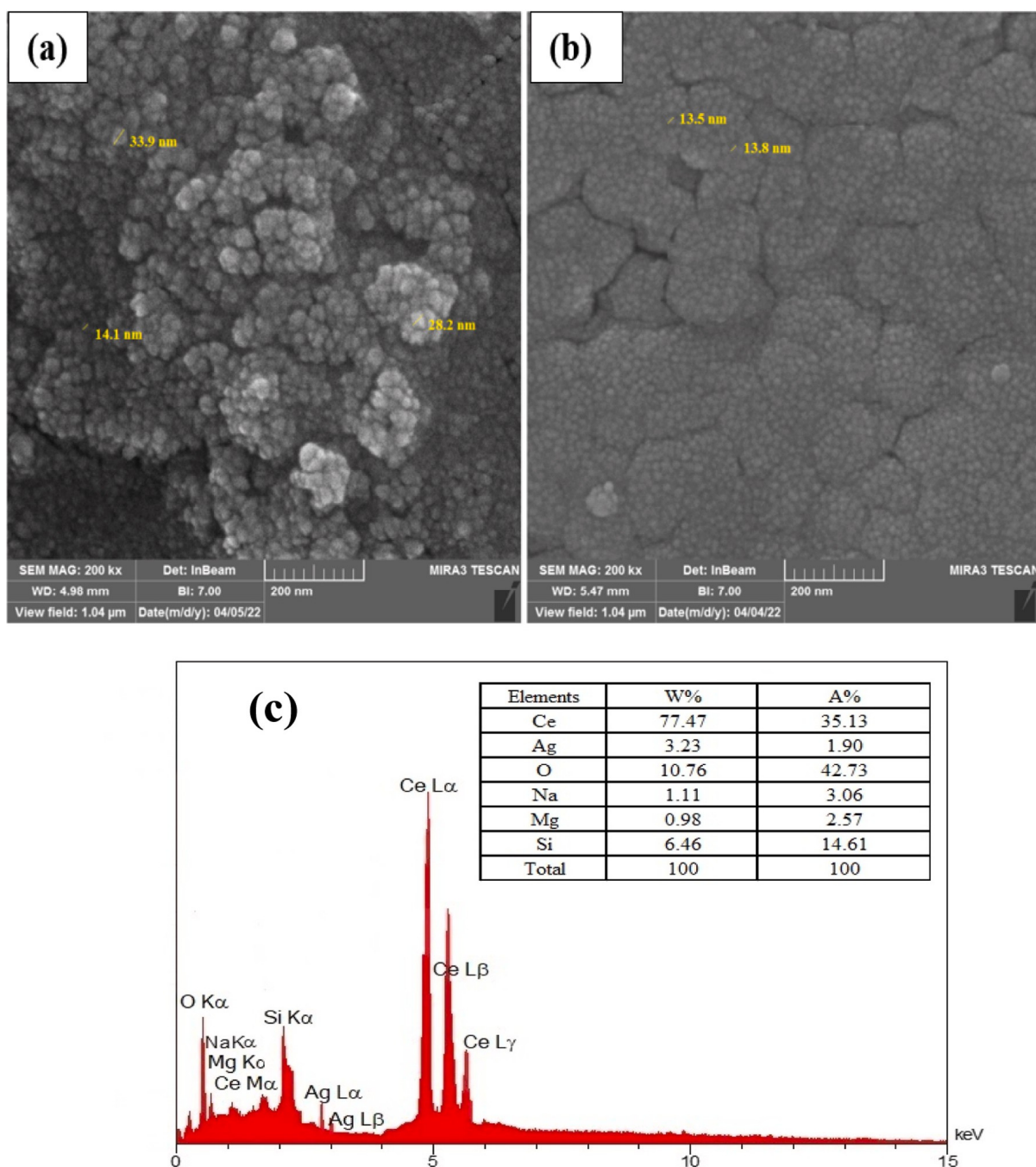


**Fig. 2.** SEM images of (a) as-deposited CeO<sub>2</sub> (b) CeO<sub>2</sub>:Ag and (c) EDS analysis of the CeO<sub>2</sub>:Ag film.

The optical absorption spectra and Tauc plots for the CeO<sub>2</sub> and CeO<sub>2</sub>:Ag thin films are shown in Figures 4a and 4b, respectively. The absorption spectrum of undoped CeO<sub>2</sub> (Fig. 4a) exhibits strong absorption around 400 nm, followed by a steep decline up to 500 nm and a gradual decrease thereafter. Upon doping with Ag NPs, a notable blue shift toward shorter wavelengths is observed, along with a decrease in overall absorbance. This shift indicates an increase in the optical band gap and is attributed to the reduced grain



size and the influence of Ag nanoparticles, which modify the film's electronic structure and light absorption behavior [26,27]. The Tauc plot (Fig. 4b), based on extrapolating the linear portion of the  $(\alpha h\nu)^2$  versus  $h\nu$  graph, reveals an increase in the energy band gap from 2.6 eV for undoped CeO<sub>2</sub> to 2.9 eV for the Ag-doped film. According to prior studies, such band gap variations are closely tied to structural changes in the semiconductor [28], which aligns with the XRD results confirming structural modification upon Ag incorporation.

The observed increase in energy bandgap upon Ag doping may be attributed to two main factors. First, the incorporation of Ag NPs into the CeO<sub>2</sub> lattice introduces a certain degree of disorder and increases the density of localized states, which can influence the electronic structure and widen the bandgap [29]. Second, the reduction in CeO<sub>2</sub> particle size caused by Ag inclusion leads to a quantum confinement effect, contributing to the increase in bandgap energy [30]. This trend aligns with earlier findings reported for CeO<sub>2</sub> doped with cadmium [31] and cobalt ions [32]. Photoluminescence (PL) spectra of the as-deposited CeO<sub>2</sub> and CeO<sub>2</sub>:Ag thin films are shown in Figures 3a and 3b, respectively, using an excitation wavelength of 280 nm. As illustrated in Figure 3a, the PL emission from pure CeO<sub>2</sub> spans the range of 330–650 nm, with distinct peaks at 340.76 nm, 374.65 nm, 479.25 nm, and 566.33 nm. These peaks, fitted using overlapping Gaussian curves, reflect various radiative transitions. Emission lines at 340.76 nm, 374.65 nm, and 479.25 nm are attributed to near-band-edge recombination of free or localized excitons [33]. The green emission at 566.33 nm is associated with surface defects, particularly oxygen vacancies, which contribute significantly to PL intensity [34].

The PL spectrum of the Ag-doped CeO<sub>2</sub> film (Fig. 3b) reveals additional emission peaks at 335.01 nm, 358.22 nm, 393.44 nm, 424.87 nm, and 506.01 nm. The incorporation of silver introduces new localized states near the conduction band edge, giving rise to these new emission features. Compared to undoped CeO<sub>2</sub>, the emission peaks in the doped sample are generally blue-shifted indicating a widened bandgap and show reduced intensity. This reduction in PL intensity suggests suppressed radiative recombination, likely due to improved charge separation or enhanced non-radiative pathways. The results from FE-SEM and XRD confirm a reduced particle size, supporting the role of quantum confinement in both the optical and electronic behavior of the Ag-doped CeO<sub>2</sub> films.

The photoluminescence data for the Ag-doped sample indicates a higher rate of electron–hole recombination under photoexcitation. Typically, a higher PL intensity correlates with a lower photocatalytic efficiency, as it reflects increased radiative recombination of charge carriers rather than their participation in surface reactions [35]. Therefore, the relatively strong PL emission from the Ag-doped CeO<sub>2</sub> suggests reduced charge transfer efficiency. It summarizes the key photoluminescence parameters of the fabricated thin films, including the emission peak wavelengths ( $\lambda$ ), full width at half maximum ( $\Delta\lambda$ ), and corresponding peak intensities (IPL).

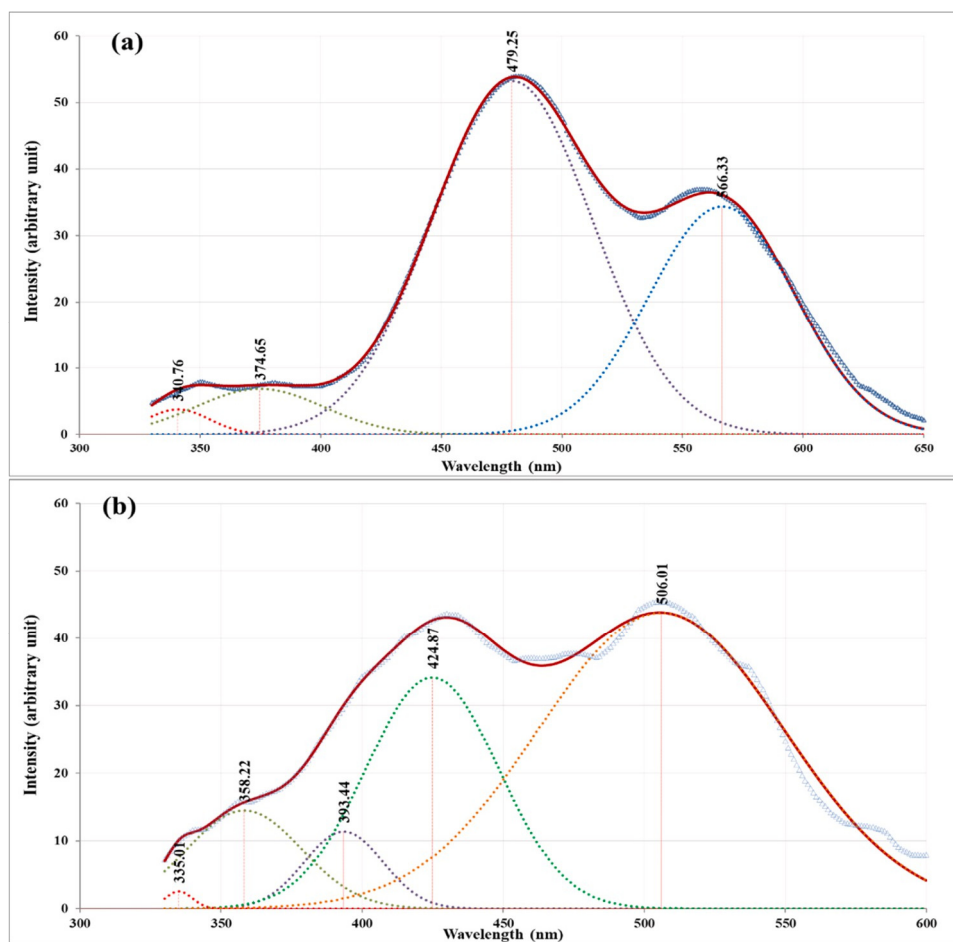


**Fig. 3.** Photoluminescence emission of (a) undoped  $\text{CeO}_2$  and (b)  $\text{CeO}_2:\text{Ag}$  thin films.

### Current Voltage (I–V) Characteristics

The current voltage behavior of the undoped  $\text{CeO}_2$  and Ag-doped  $\text{CeO}_2$  thin films, both in dry air and under exposure to 5 ppm  $\text{NO}_2$  at 25 °C, is presented in Figure 4. As shown in Figures 4a and 4b, the electrical current increases with applied voltage, which is attributed to the migration of oxygen vacancies toward the metal semiconductor interface, enhancing charge transport. Both films exhibit rectifying diode-like behavior within the  $\pm 3$  V voltage range, indicating the influence of  $\text{NO}_2$  gas on the electrical characteristics of the sensing layer.

Upon exposure to  $\text{NO}_2$ , an increase in electrical conductivity was observed for both films due to a rise in free charge carriers at the sensor surface. This indicates an effective interaction between  $\text{NO}_2$  molecules and the sensing material. Notably, the  $\text{CeO}_2:\text{Ag}$  film exhibits a higher current response compared to pure  $\text{CeO}_2$ , as shown in Figure 4b. This enhancement is ascribed to the increased carrier density facilitated by the incorporation of Ag nanoparticles.

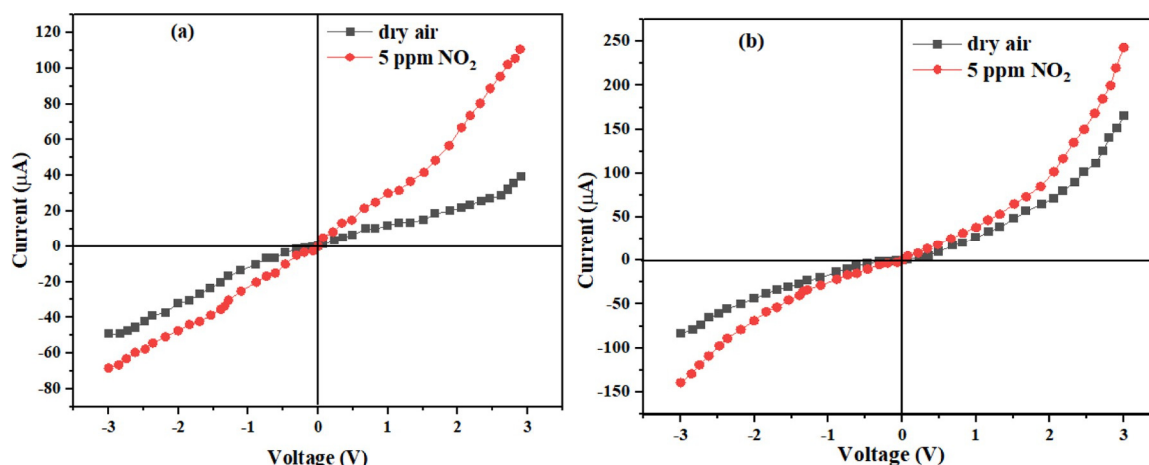


**Fig. 4.** *I-V* characteristics of (a)  $\text{CeO}_2$  and (b)  $\text{CeO}_2\text{:Ag}$  thin films in dry air and when exposed to 5 ppm  $\text{NO}_2$  at 25 °C.

### Gas Sensing Performance

It is well established that heterostructures formed by combining different materials can significantly improve the surface physicochemical properties of gas sensors [37]. In this context, the gas sensing performance of both pure  $\text{CeO}_2$  and  $\text{CeO}_2\text{:Ag}$  thin films was evaluated toward  $\text{NO}_2$  detection to highlight the synergistic effect of the composite structure. The influence of operating temperature on sensor response was studied by exposing both films to 5 ppm of  $\text{NO}_2$  across a temperature range from room temperature (25 °C) to 350 °C in 50 °C increments. As illustrated in Figure 5, the  $\text{CeO}_2\text{:Ag}$  sensor exhibited a markedly enhanced response compared to the undoped  $\text{CeO}_2$  film, demonstrating the effectiveness of Ag doping in improving sensitivity. Interestingly, the highest sensor response for both films was observed at 25 °C, with a sharp decline at elevated temperatures. This reduction in response at higher temperatures is likely due to reduced physisorption of water molecules, which plays a role in the detection of oxidizing gases like  $\text{NO}_2$  [38]. Additionally, at elevated temperatures, the rapid desorption of analyte gas molecules may outpace their surface reaction rates, diminishing the overall sensor response [39].

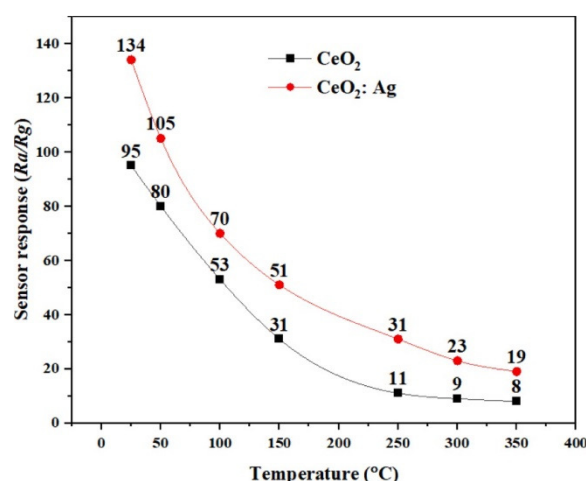


**Fig. 5.** The response of the  $\text{CeO}_2$  and  $\text{CeO}_2\text{:Ag}$  sensors at various operating temperatures.



## Gas Sensing Mechanism and Response Analysis

The change in electrical resistance of a gas sensor upon exposure to an analyte gas is governed by the interaction between the gas molecules and the sensor surface, and is influenced by both the type of the predominant charge carrier in the sensing material and the chemical nature of the target gas whether reducing or oxidizing. In general, oxidizing gases such as  $\text{NO}_2$  act as electron acceptors. As a result, they tend to increase the resistance in n-type semiconductors and decrease it in p-type semiconductors [40]. Figure 6 illustrates the time-dependent resistance behavior of  $\text{CeO}_2$  and  $\text{CeO}_2:\text{Ag}$  thin-film sensors upon exposure to 5 ppm  $\text{NO}_2$ . Upon gas exposure (Gas ON), the resistance of both sensors drops significantly, and when the gas flow is halted (Gas OFF), the resistance returns to its original value. This characteristic decrease in resistance upon exposure to an oxidizing gas is typical of p-type semiconductors [41].

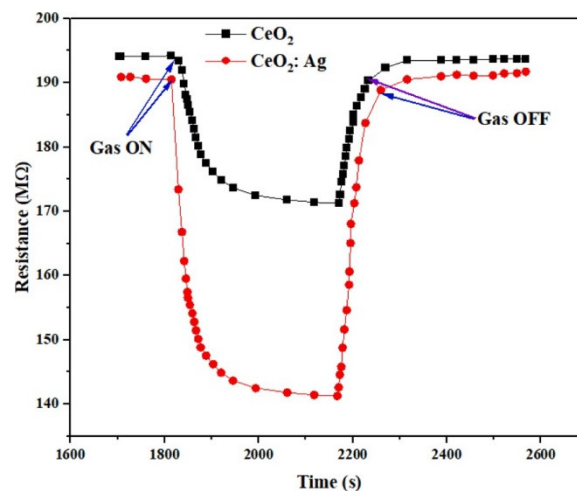


**Fig. 6.** Dynamic changes in the electrical resistance of  $\text{CeO}_2$  and  $\text{CeO}_2:\text{Ag}$  thin films.

This response can be explained by the adsorption and ionization of oxygen molecules on the sensor's surface in ambient air. These adsorbed oxygen species ( $\text{O}^-$ ,  $\text{O}_2^-$ , or  $\text{O}_2^{2-}$ ) extract electrons from the conduction band, creating a surface potential barrier and an electron depletion layer at the grain boundaries, as shown in Figure 7 [42]. When exposed to  $\text{NO}_2$ , the gas further withdraws electrons from the surface, leading to an increase in hole concentration (majority carriers in p-type materials) and, consequently, a decrease in electrical resistance [43]. The sensing measurements revealed that the undoped  $\text{CeO}_2$  film exhibited a 95% response, with a response time of 96 seconds and a fast recovery time of 3 seconds. Upon doping with Ag nanoparticles, the  $\text{CeO}_2:\text{Ag}$  sensor showed a significantly enhanced response of 134%, with a reduced response time of 67 seconds and a slightly increased recovery time of 15 seconds.

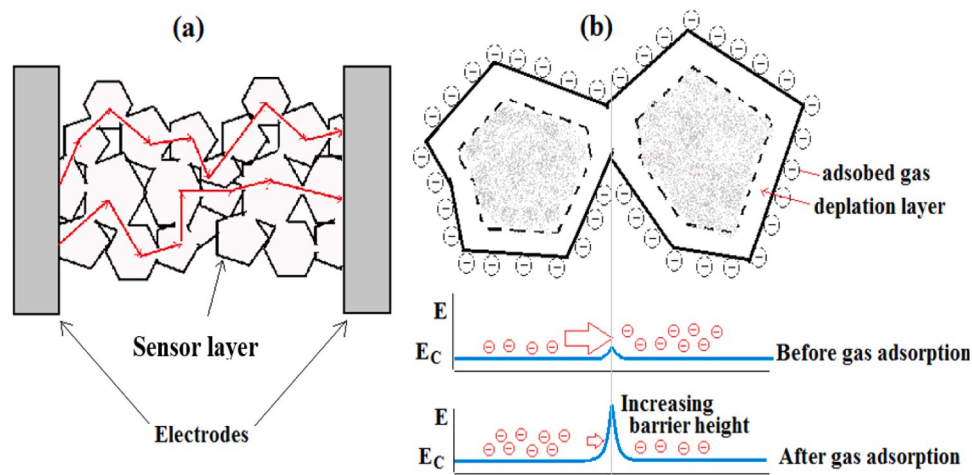


**Fig. 7.** Schematic of (a) the sensor layer and (b) the gas sensitivity mechanism.

This performance improvement can be attributed to the formation of a metal semiconductor junction (Schottky barrier) between the Ag nanoparticles and  $\text{CeO}_2$ . In such junctions, as depicted in Figure 8a, the metal's conduction band aligns with the Fermi level, while in the semiconductor, the valence and conduction bands are separated by a bandgap. When Ag is introduced, electrons can transfer from  $\text{CeO}_2$  to Ag, leading to band bending and facilitating more efficient charge separation and transfer. This interfacial interaction enhances the sensitivity of the sensor by promoting more active sites for  $\text{NO}_2$  adsorption and accelerating the charge transport process.

The Fermi level of the semiconductor is higher than that of the metal, as illustrated in Figure 8a. This indicates that electrons in the semiconductor occupy higher energy states compared to those in the metal. When a Schottky junction is formed between the semiconductor and the metal, electrons naturally flow from the semiconductor to the metal until thermal equilibrium is achieved. At this point, the Fermi levels on both sides align, as shown in Figure 8b [45]. This electron transfer results in the formation of a depletion region in the semiconductor and an accumulation layer in the metal. Furthermore, the adsorption of oxygen molecules on the sensor surface can further deplete this region by withdrawing more electrons from the semiconductor's conduction band. This process effectively narrows the conduction channel and heightens the sensor's reactivity toward target gases, ultimately enhancing gas detection performance [46].

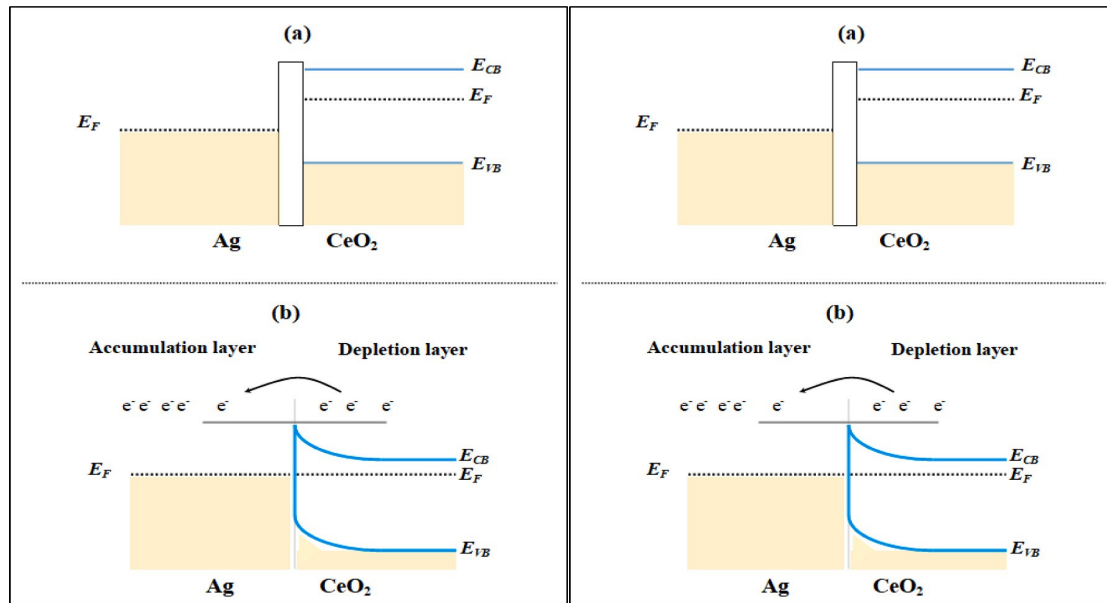


**Fig. 8.** Metal-Semiconductor energy-band diagram (a) before and (b) after the development of a Schottky junction.

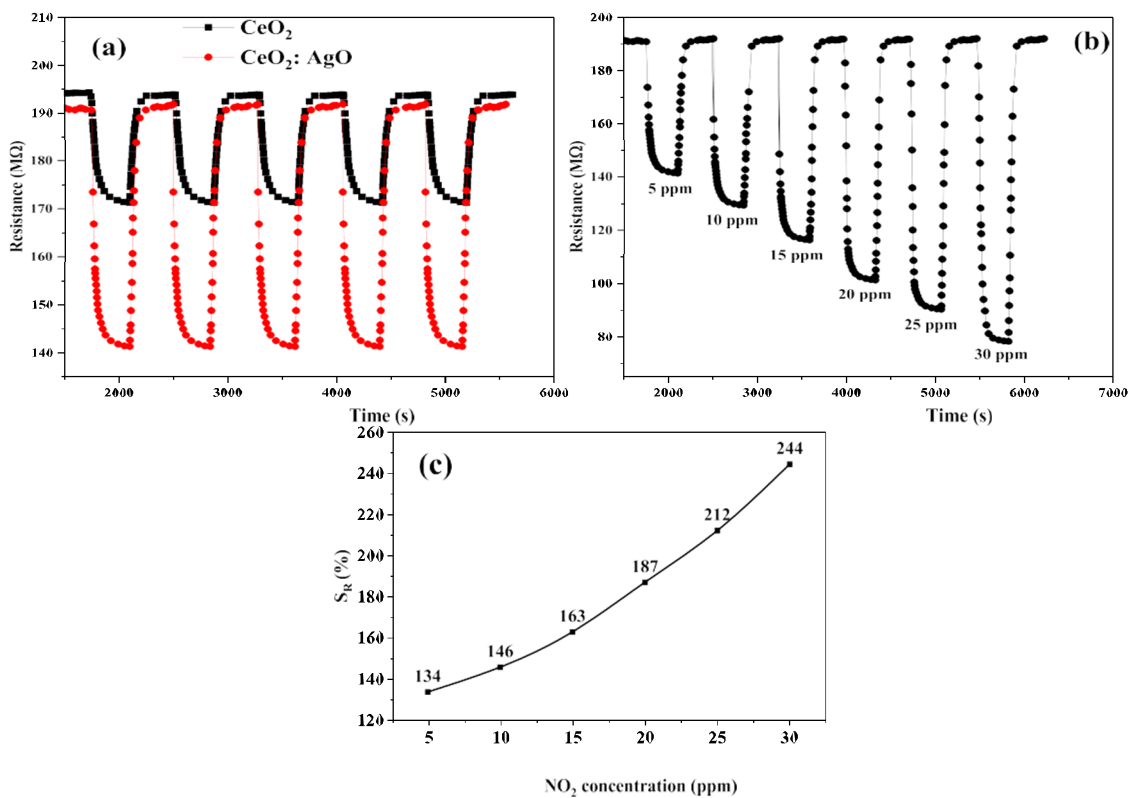


**Fig. 9.** (a) Dynamic sensing response (b) electrical resistance response of a sensor against exposure to varying  $NO_2$  concentrations (c)  $S_R$  % to various  $NO_2$  concentrations.

The repeatability of the sensor response was evaluated by cycling the CeO<sub>2</sub>:Ag sensor through five successive NO<sub>2</sub> exposure and recovery cycles at 25 °C. As shown in Figure 9a, the sensor consistently returned to its baseline resistance after each cycle, indicating that NO<sub>2</sub> adsorption was reversible and that the sensor has good reproducibility. To assess the concentration-dependent sensitivity, the CeO<sub>2</sub>:Ag sensor was tested at room temperature under various NO<sub>2</sub> concentrations ranging from 5 to 30 ppm. Figure 9b presents the dynamic response curves, which clearly show that the sensor response increases with rising NO<sub>2</sub> concentration. The sensor exhibited reliable detection down to 5 ppm NO<sub>2</sub>, demonstrating its sensitivity to low concentrations at room temperature. Figure 9c further quantifies the sensor response as a function of NO<sub>2</sub> concentration.

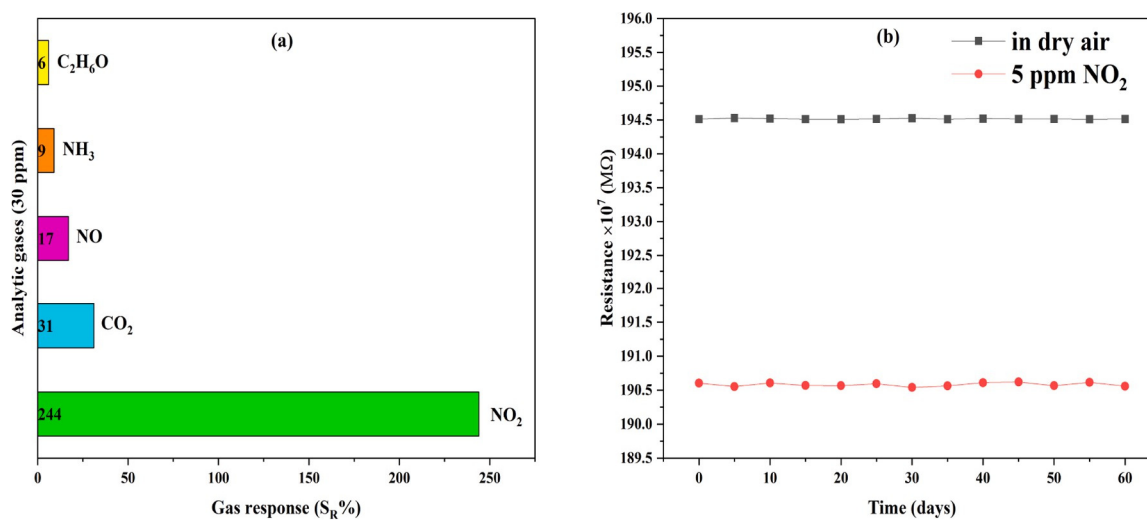


**Fig. 10.** The selectivity of the CeO<sub>2</sub>:Ag gas sensor against different types of gases at a concentration of 30 ppm and (b) sensor stability over sixteen days.

Selectivity the ability to distinguish a specific gas among other potential interferents is another critical parameter. The CeO<sub>2</sub>:Ag sensor's selectivity was examined by exposing it to 30 ppm concentrations of several gases, including CO<sub>2</sub>, NO, NH<sub>3</sub>, and ethanol (C<sub>2</sub>H<sub>6</sub>O), at 25 °C in dry air. As illustrated in Figure 10a, the response to NO<sub>2</sub> reached 244%, which is approximately 8, 14, 26, and 38 times greater than the responses to CO<sub>2</sub>, NO, NH<sub>3</sub>, and ethanol, respectively. This clearly demonstrates the sensor's superior selectivity toward NO<sub>2</sub>. The long-term stability of the CeO<sub>2</sub>:Ag sensor was also tested over a 16-day period by monitoring its performance under dry air and during exposure to 5 ppm NO<sub>2</sub> at 25 °C. As shown in Figure 10b, the sensor maintained a consistent response over time, indicating excellent stability and durability.

#### IV. CONCLUSION

The results confirm that nanostructured CeO<sub>2</sub> doped with Ag nanoparticles is an effective sensing material for NO<sub>2</sub> detection at room temperature. The enhanced sensitivity, good selectivity, repeatability, and long-term operational stability suggest that this novel material has strong potential for future practical gas sensing applications, especially in environments requiring low detection limits and low-temperature operation.

## References

- [1] J.M. Marei, A.A. Khalefa, Q.A. Abduljabbar, J.M. Rzaiz, Nitrogen dioxide gas sensor of In<sub>2</sub>O<sub>3</sub>- ZnO polyhedron nanostructures prepared by spray pyrolysis, *J. Nano Res.* 70 (2021) 41–51, <https://doi.org/10.4028/www.scientific.net/JNanoR.70.41>.
- [2] P.G. Choi, N. Izu, N. Shirahata, Y. Masuda, Improvement of sensing properties for SnO<sub>2</sub> gas sensor by tuning of exposed crystal face, *Sens. Actuators B Chem.* 296 (2019), 126655, <https://doi.org/10.1016/j.snb.2019.126655>.
- [3] J. Ma, H. Fan, W. Zhang, J. Sui, C. Wang, M. Zhang, N. Zhao, A. Kumar Yadav, W. Wang, W. Dong, S. Wang, High sensitivity and ultra-low detection limit of chlorine gas sensor based on In<sub>2</sub>O<sub>3</sub> nanosheets by a simple template method, *Sens. Actuators B Chem.* 305 (2020), 127456, <https://doi.org/10.1016/j.snb.2019.127456>.
- [4] J.H. Bang, M.S. Choi, A. Mirzaei, S. Han, H.Y. Lee, S.-W. Choi, S.S. Kim, H.W. Kim, Hybridization of silicon nanowires with TeO<sub>2</sub> branch structures and Pt nanoparticles for highly sensitive and selective toluene sensing, *Appl. Surf. Sci.* 525 (2020), 146620, <https://doi.org/10.1016/j.apsusc.2020.146620>.
- [5] W. Jiang, L. Meng, S. Zhang, X. Chuai, Z. Zhou, C. Hu, P. Sun, F. Liu, X. Yan, G. Lu, Design of highly sensitive and selective xylene gas sensor based on Ni-doped MoO<sub>3</sub> nano-pompon, *Sens. Actuators B Chem.* 299 (2019), 126888, <https://doi.org/10.1016/j.snb.2019.126888>.
- [6] X. Wang, T. Wang, G. Si, Y. Li, S. Zhang, X. Deng, X. Xu, Oxygen vacancy defects engineering on Ce-doped  $\alpha$ -Fe<sub>2</sub>O<sub>3</sub> gas sensor for reducing gases, *Sens. Actuators B Chem.* 302 (2020), 127165, <https://doi.org/10.1016/j.snb.2019.127165>.
- [7] V. Manikandan, R. Marnadu, J. Chandrasekaran, S. Vigneselvan, R.S. Mane, C.E. Banks, A. Mirzaei, Inherent characteristics of ultra-photosensitive Al/Cu–CeO<sub>2</sub>/p-Si metal oxide semiconductor diodes, *J. Mater. Chem. C* 10 (2022) 1445–1457, <https://doi.org/10.1039/D1TC05630A>.
- [8] H. Pourrahmani, M. Matian, J. Van herle, Poisoning effects of cerium oxide (CeO<sub>2</sub>) on the performance of proton exchange membrane fuel cells (PEMFCs), *ChemEngineering* 6 (2022) 36, <https://doi.org/10.3390/chemengineering6030036>.
- [9] Y. Wen, Q. Huang, Z. Zhang, W. Huang, Morphology-dependent catalysis of CeO<sub>2</sub>- based nanocrystal model catalysts, *Chin. J. Chem.* 40 (2022) 1856–1866, <https://doi.org/10.1002/cjoc.202200147>.
- [10] A.B. Shcherbakov, V.V. Reukov, A.V. Yakimansky, E.L. Krasnopeeva, O.S. Ivanova, A.L. Popov, V.K. Ivanov, CeO<sub>2</sub> nanoparticle-containing polymers for biomedical applications: a review, *Polymres* 13 (2021) 924, <https://doi.org/10.3390/polym13060924>.
- [11] F. Zhang, P. Wang, J. Koberstein, S. Khalid, S.-W. Chan, Cerium oxidation state in ceria nanoparticles studied with X-ray photoelectron spectroscopy and absorption near edge spectroscopy, *Surf. Sci.* 563 (2004) 74–82, <https://doi.org/10.1016/j.susc.2004.05.138>.
- [12] A. Miri, M. Sarani, M. Khatami, Nickel-doped cerium oxide nanoparticles: biosynthesis, cytotoxicity and UV protection studies, *RSC Adv.* 10 (2020) 3967–3977, <https://doi.org/10.1039/c9ra09076b>.
- [13] B.-H. Chen, B. Stephen Inbaraj, Various physicochemical and surface properties controlling the bioactivity of cerium oxide nanoparticles, *Crit. Rev. Biotechnol.* 38 (2018) 1003–1024, <https://doi.org/10.1080/07388551.2018.1426555>.
- [14] C. Gunawan, M.S. Lord, E. Lovell, R.J. Wong, M.S. Jung, D. Oscar, R. Mann, R. Amal, Oxygen-vacancy engineering of cerium-oxide nanoparticles for antioxidant activity, *ACS Omega* 4 (2019) 9473–9479, <https://doi.org/10.1021/acsomega.9b00521>.
- [15] A.A. Aboud, H. Al-Kelesh, W.M.A.El Roubi, A.A. Farghali, A. Hamdedein, M. H. Khedr, CO<sub>2</sub> responses based on pure and doped CeO<sub>2</sub> nano-pellets, *J. Mater. Res. Technol.* 7 (2018) 14–20, <https://doi.org/10.1016/j.jmrt.2017.03.003>.
- [16] P. Nowak, W. Maziarz, A. Rydosz, K. Kowalski, M. Ziabka, K. Zakrzewska, SnO<sub>2</sub>/ TiO<sub>2</sub> thin film n-n heterostructures of improved sensitivity to NO<sub>2</sub>, *Sensors* 20 (2020) 6830, <https://doi.org/10.3390/s20236830>.
- [17] T.-Y. Lai, G.-C. Chen, Y.-J. Hsia, Micro-electromechanical system gas sensors based on CeO<sub>2</sub>



- nanoparticles, *Sens. Mater.* 35 (2023) 1141–1148, <https://doi.org/10.18494/SAM4239>.
- [18] D.N. Oosthuizen, D.E. Motaung, H.C. Swart, Gas sensors based on CeO<sub>2</sub> nanoparticles prepared by chemical precipitation method and their temperature- dependent selectivity towards H<sub>2</sub>S and NO<sub>2</sub> gases, *Appl. Surf. Sci.* 505 (2020), 144356, <https://doi.org/10.1016/j.apsusc.2019.144356>.
- [19] L. Zhang, Q. Fang, Y. Huang, K. Xu, P.K. Chu, F. Ma, Oxygen vacancy enhanced gas-sensing performance of CeO<sub>2</sub>/graphene heterostructure at room temperature, *Anal. Chem.* 90 (2018) 9821–9829, <https://doi.org/10.1021/acs.analchem.8b01768>.
- [20] K. Sun, G. Zhan, H. Chen, S. Lin, Low-operating-temperature NO<sub>2</sub> sensor based on a CeO<sub>2</sub>/ZnO heterojunction, *Sensors* 21 (2021) 8269, <https://doi.org/10.3390/s21248269>.
- [21] L. Zhang, Q. Fang, Y. Huang, K. Xu, F. Ma, P.K. Chu, Facet-engineered CeO<sub>2</sub>/graphene composites for enhanced NO<sub>2</sub> gas-sensing, *J. Mater. Chem. C* 5 (2017) 6973–6981, <https://doi.org/10.1039/C7TC01523B>.
- [22] D. Majumder, S. Roy, Development of low-ppm CO sensors using pristine CeO<sub>2</sub> nanospheres with high surface area, *ACS Omega* 3 (2018) 4433–4440, <https://doi.org/10.1021/acsomega.8b00146>.
- [23] H. Li, Y. Qu, X. Zhang, The gas sensor utilizing CeO<sub>2</sub> nanorods for the low temperature detection of hydrogen, *Inorg. Chem. Commun.* 130 (2021), 108692, <https://doi.org/10.1016/j.inoche.2021.108692>.
- [24] N. Jayababu, M. Poloju, J. Shruthi, M.V.R. Reddy, NiO decorated CeO<sub>2</sub> nanostructures as room temperature isopropanol gas sensors, *RSC Adv.* 9 (2019) 13765–13775, <https://doi.org/10.1039/C9RA00441F>.
- [25] K. Jalaiah, K.C. Mouli, K.V. Babu, R.V. Krishnaiah, Structural, electrical and magnetic properties of Mg-Zr co-substituted Ni<sub>0.5</sub>Zn<sub>0.5</sub>Fe<sub>2</sub>O<sub>4</sub>, *J. Sci. Adv. Mater. Devices* 4 (2019) 310–318.
- [26] S. Chahal, S. Singh, A. Kumar, P. Kumar, Oxygen-deficient lanthanum doped cerium oxide nanoparticles for potential applications in spintronics and photocatalysis, *Vacuum* 177 (2020), 109395, <https://doi.org/10.1016/j.vacuum.2020.109395>.
- [27] P.N. Mishra, P.K. Mishra, D. Pathak, The influence of Al doping on the optical characteristics of ZnO nanopowders obtained by the low-cost sol-gel method, *Chemistry* 4 (2022) 1136–1146, <https://doi.org/10.3390/chemistry4040077>.
- [28] N.T. Latif, J.M. Rzaiz, Concentration effect of mixed SnO<sub>2</sub>-ZnO on TiO<sub>2</sub> optical properties thin films prepared by chemical spray pyrolysis technique, *J. Univ. Anbar Pure Sci.* 14 (2022) 43–49, <https://doi.org/10.37652/juaps.2022.172320>.
- [29] L.R. Singh, M.A. Hussain, Effect of doping concentration on the optical properties of nanocrystalline zn doped pbs thin films deposited by cbd method, *Chalcogenide Lett.* 17 (2020) 583–591, <https://doi.org/10.15251/CL.2020.1711.583>.
- [30] C. De Mello Donegá, *Nanoparticles: Workhorses of Nanoscience*, Springer, Verlag Berlin Heidelberg, 2014. <https://doi.org/10.1007/978-3-662-44823-6>.
- [31] S. Gnanam, V. Rajendran, Facile sol-gel preparation of Cd-doped cerium oxide (CeO<sub>2</sub>) nanoparticles and their photocatalytic activities, *J. Alloy. Compd.* 735 (2018) 1854–1862, <https://doi.org/10.1016/j.jallcom.2017.11.330>.
- [32] Y.A. Syed Khadar, A. Balamurugan, V.P. Devarajan, R. Subramanian, S. Dinesh Kumar, Synthesis, characterization and antibacterial activity of cobalt doped cerium oxide (CeO<sub>2</sub>:Co) nanoparticles by using hydrothermal method, *J. Mater. Res. Technol.* 8 (2019) 267–274, <https://doi.org/10.1016/j.jmrt.2017.12.005>.
- [33] A. Arumugam, C. Karthikeyan, A.S. Haja Hameed, K. Gopinath, S. Gowri, V. Karthika, Synthesis of cerium oxide nanoparticles using *Gloriosa superba* L. leaf extract and their structural, optical and antibacterial properties, *Mater. Sci. Eng. C* 49 (2015) 408–415, <https://doi.org/10.1016/j.msec.2015.01.042>.
- [34] J. Milanez, A.T. de Figueiredo, S. de Lazaro, V.M. Longo, R. Erlo, V.R. Mastelaro, R. W.A. Franco, E. Longo, J.A. Varela, The role of oxygen vacancy in the photoluminescence property at room temperature of the CaTiO<sub>3</sub>, *J. Appl. Phys.* 106 (2009), 043526, <https://doi.org/10.1063/1.3190524>.

- [35] X.-J. Wen, C.-G. Niu, L. Zhang, C. Liang, G.-M. Zeng, A novel Ag<sub>2</sub>O/CeO<sub>2</sub> heterojunction photocatalysts for photocatalytic degradation of enrofloxacin: possible degradation pathways, mineralization activity and an in depth mechanism insight, *Appl. Catal. B Environ.* 221 (2018) 701–714, <https://doi.org/10.1016/j.apcatb.2017.09.060>.
- [36] J.M. Rzaiz, N.F. Habubi, Enhancing the CO<sub>2</sub> sensor response of nickel oxide-doped tin dioxide thin films synthesized by SILAR method, *J. Mater. Sci. Mater. Electron.* 33 (2022) 11851–11863, <https://doi.org/10.1007/s10854-022-08148-2>.
- [37] H. Li, B. Ding, J. Wu, Q. Lv, Synthesis of MoO<sub>3</sub>/NiO nanolamella and their enhanced hydrogen sensing performance, *Inorg. Chem. Commun.* 145 (2022), 109967, <https://doi.org/10.1016/j.inoche.2022.109967>.
- [38] P. Nowak, W. Maziarz, A. Rydosz, K. Kowalski, M. Ziabka, K. Zakrzewska, SnO<sub>2</sub>/TiO<sub>2</sub> thin film n-n heterostructures of improved sensitivity to NO<sub>2</sub>, *Sensors* 20 (2020) 1–20, <https://doi.org/10.3390/s20236830>.
- [39] J. Chen, J. Zhang, M. Wang, Y. Li, High-temperature hydrogen sensor based on platinum nanoparticle-decorated SiC nanowire device, *Sens. Actuators B Chem.* 201 (2014) 402–406, <https://doi.org/10.1016/j.snb.2014.04.068>.
- [40] M. Donarelli, M. Ferroni, A. Ponzoni, F. Rigoni, D. Zappa, C. Baratto, G. Faglia, E. Comini, G. Sberveglieri, Single metal oxide nanowire devices for ammonia and other gases detection in humid atmosphere, *Procedia Eng.* 168 (2016) 1052–1055, <https://doi.org/10.1016/j.proeng.2016.11.338>.
- [41] Q.A. Abduljabbar, H.A. Radwan, J.M. Marei, J.M. Rzaiz, Spray rate effects on the NO<sub>2</sub> gas sensor properties of Ni-doped SnO<sub>2</sub> nanoflakes, *Eng. Res. Express* 4 (2022), 015028, <https://doi.org/10.1088/2631-8695/ac57fb>.
- [42] H.A. Radwan, J.M. Marei, A.A. Khalefa, J.M. Rzaiz, ZnO/PSi nanoparticles thin film for NO<sub>2</sub> sensing application prepared by pulsed laser deposition, *Indian J. Phys.* (2023), <https://doi.org/10.1007/s12648-023-02806-9>.
- [43] T. Akamatsu, T. Itoh, N. Izu, W. Shin, NO and NO<sub>2</sub> sensing properties of WO<sub>3</sub> and Co<sub>3</sub>O<sub>4</sub> based gas sensors, *Sensors* 13 (2013) 12467–12481, <https://doi.org/10.3390/s130912467>.
- [44] I.M. Ibrahim, J.M. Rzaiz, A. Ramizy, Characterization OF CuPcTs/PS for NO<sub>2</sub> gas sensor, *Dig. J. Nanomater. Biostruct.* 12 (2017) 1187–1196.
- [45] S. Arumugam, M. Perumal, K.P. Anjana, S.V.M. Satyanarayna, S.K. Sinha, Plasma–metal junction, *Phys. Plasmas* 27 (2020), 023512, <https://doi.org/10.1063/1.5125618>.
- [46] A. Bag, N.-E. Lee, Gas sensing with heterostructures based on two-dimensional nanostructured materials: a review, *J. Mater. Chem. C* 7 (2019) 13367–13383, <https://doi.org/10.1039/C9TC04132J>.